Transmission Loss of a Labyrinthine Acoustic Metamaterial Augmented with Multichannel Feedforward Active Noise Control

Gregory M. Hernandez* and Jordan Cheer†
Institute of Sound and Vibration Research, University of Southampton (UK) ‡

Gianluca Memoli§
AURORA Project, School of Engineering and Informatics, University of Sussex (UK)¶
(Dated: March 17, 2026)

Acoustic metamaterials and active noise control are two advanced noise control treatments that can typically offer performance that exceeds that of conventional passive noise control treatments. Acoustic metamaterials utilize sub-wavelength structures to realize sound field control, whilst active noise control treatments achieve control via the introduction of additional acoustic sources driven to generate a secondary sound field that interferes in a controlled way with the original, primary sound field. This paper presents an investigation into combining these two noise control techniques to achieve enhanced noise control over a spatial region using a "hybrid" device. In particular, conventional feedforward active noise control is combined with a labyrinthine metasurface and the increase in performance offered by the hybrid solution is demonstrated.

I. INTRODUCTION

Industrial noise has had an impact on human society since the industrial revolution, and it is now well accepted that this pollutant presents a significant cost to society due to its negative health effects [1]. For many centuries, acoustical engineers had two principle methods of managing noise: mass-based solutions and acoustic absorbers [2]. Unless resonators are used, these two methods require a large spatial footprint or mass to achieve noise control at the lower frequencies typical of industrial settings and ventilation systems.

Active Noise Control (ANC), whose first commercial applications emerged in the 1980s [3], offers a solution to overcome the low frequency limitations of conventional passive noise control treatments in a variety of applications including headphones [3], road vehicles [4] or aircraft [5]. There are a variety of physical aspects that limit the potential application of ANC systems, but when the objective is to achieve sound field control over an extended spatial domain the number of secondary sources, or control loudspeakers, rapidly increases with both frequency and size of the region over which control is desired [6]. This increases both the complexity and the cost of utilizing an active system and, therefore, their use is often limited to high performance, critical applications.

An alternative solution to overcoming the limitations of conventional passive noise control treatments is offered by acoustic metamaterials [7–9]. Typically subwavelength, these structures exhibit an effective bulk modulus and mass density that can facilitate sound field manipulation and enable techniques such as beamforming [10] or acoustic cloaking [11] to be realized. Various acoustic metamaterial designs have been proposed that are able to achieve effective sound attenuation at low frequencies. For example, in [8] an array of resonators is used to form a metasurface that achieves 99% energy absorption at 511 Hz with a surface thickness of about $\lambda/20$, where λ is the acoustic wavelength; in [12], space coiling is used to realize perfect absorption at 125 Hz with a thickness of about $\lambda/223$; and in [13], a membrane-type acoustic metamaterial is shown to achieve perfect absorption at 152 Hz with a thickness of around $\lambda/133$. These various metamaterial devices, however, have two key limitations: they are effective only over a limited bandwidth and can be challenging to mass manufacture. Overcoming these two limitations has led to significant research effort in both the manufacture and application of metamaterials [14]. However, real-world application has remained somewhat limited, with only a few examples of metamaterials applied in practice [15–17]. Despite extensive development, and emerging commercial exploitation [17], the utilization of passive metamaterials for dynamic applications remains challenging.

To address the challenge posed by dynamic applications, various researchers have proposed active acoustic metamaterial solutions for wave control [18–21], however, they are typically rather complex to implement and the cost may be prohibitive for many applications. To reach a balance between performance under dynamic applications and complexity, previous research has also explored the integration of ANC techniques with a passive Helmholtz resonator based metamaterial [22]. This hybrid active-passive solution demonstrated a 10 dB enhancement in transmission loss compared to either the passive or active systems operating in isolation, and achieved more than a factor of eight increase in the bandwidth compared to the passive resonator-based metamaterial. Combining passive metamaterial performance with active control has also been explored in [23], where

---

* gregory.hernandez@duke.edu
† j.cheer@soton.ac.uk
‡ Also at Duke University.
§ g.memoli@sussex.ac.uk
¶ Also at Metasonixx Ltd, Brighton (UK).

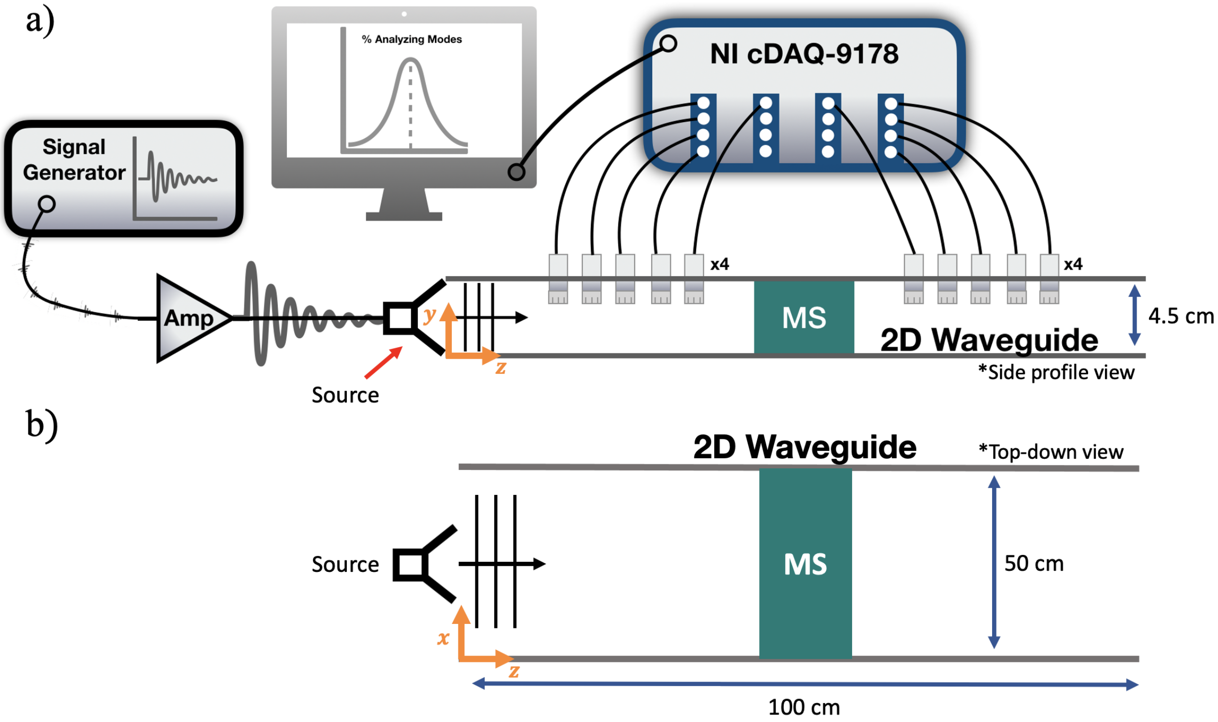

FIG. 1: (a) The side profile view of the experimental setup, showing the 2D rectangular waveguide, the 20 microphones upstream and 20 microphones downstream of the metasurface (MS), the data acquisition system used to record the microphone signals, the computer used to process these signals, and the signal generator used to drive the primary loudspeakers via an amplifier with Gaussian white noise. The primary loudspeaker are positioned variously at discrete locations across the width of the duct. (b) The top-down view of the waveguide, showing the MS and the primary source location. Note that the term 2D in this text, with respect to the waveguide, refers to the xz-plane: modes along the x-dimension can propagate in the z-direction.

an active control strategy is combined with a membrane-type acoustic metamaterial to tune the frequency over which a high level of sound transmission loss is achieved.

In this work, an alternative hybrid active-passive acoustic metamaterial is investigated, which is realized by combining a multichannel feedforward ANC system with a static acoustic metasurface realized using the labyrinthine metamaterial unit cells described in [10]. The objective here is to enhance the downstream attenuation performance of the metasurface by using ANC, and thus demonstrate the benefits of a hybrid approach, providing useful insights for future development of similar hybrid metamaterials. Notably, the hybrid system is evaluated in a 2D waveguide (xz-plane), which goes beyond the 1D waveguide investigations used in much of the literature [19, 22]. The paper is structured as follows: Section II describes the physical system, including the labyrinthine metasurface and the loudspeakers and microphones utilized to implement the active control system; Section III presents the passive performance of the metasurface; Section IV presents the performance of both the ANC system alone and when combined in various ways with the passive metasurface to realize different hybrid systems; finally, Section V presents conclusions.

II. EXPERIMENTAL CONSTRUCTION

The experimental apparatus is depicted in Fig. 1a and 1b. The 2D waveguide, which is 100 cm long, 50 cm wide, and 4.5 cm tall, is constructed from 5 mm thick rigid engineering plastic (polyamide 66). The lateral walls of the waveguide are screwed to both the top and bottom plates and further secured with epoxy to the bottom plate.

A. Labyrinthine Metasurface

The considered metasurface, denoted MS in Fig. 1, has been realized using the concept of "metamaterial bricks" introduced by Memoli *et al.* [10]. This previous work demonstrated that, once the main frequency of operation has been selected, most narrow-band metasurfaces can be built by reconfiguring 16 labyrinthine pre-defined metamaterial bricks, each encoding a specific phase shift between 0 and $15/8\pi$. In [10], the metamaterial bricks have a length of λ in the direction of propagation, which will be referred to as the "thickness" of the device, and are $\lambda/2$ wide in the other two dimensions. However, these cells were considered too large for the current setup. At

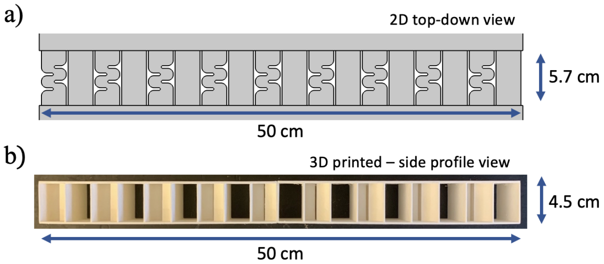

FIG. 2: (a) The 2D top-down perspective of the metamaterial unit cells situated in the waveguide. (b) The 3D-printed metamaterial constructed of PLA plastic. There are a total of 18 unit cells: 9 are open units, the other 9 are labyrinthine unit cells.

2400 Hz the unit cells would have been 14.3 cm thick and 7.14 cm in the lateral dimensions. Therefore, the metamaterial bricks presented in [24] have been used here, which have a thickness of $\lambda/3$, a lateral dimension of $\lambda/6$, and encode a phase delay ranging from 0 to $15/8\pi$.

The metasurface (a configured array of metamaterial structures) used in this experiment contains 18 unit cells, constructed of PLA plastic, giving a total width of 50 cm and a thickness of ≈ 4.76 cm. The 2D blueprints in [24] were elongated to fit the waveguide, so that the final height of the metasurface was 4.5 cm. The thickness of the metasurface was 5.7 cm (40% or $2\lambda/5$ in air), with a physical wall construction thickness of 2 mm to ensure an effective connection with the loudspeaker (LS) array structure (see Section II B 1) and to ensure that the structure was sufficiently rigid to avoid structural effects.

The metasurface has been constructed from two distinct metamaterial bricks, which are arranged in an alternating pattern, as shown in Fig. 2. This two unit cell architecture (analogous to a dipole pair) is the basis of the metasurface design used here. At the selected frequency of 2400 Hz, one unit cell is an open channel (phase shift: 0), through which the incident wave travels without any change in phase. The other unit cell is a meandering, or labyrinthine cell, designed to create a phase shift of π, so that the wave that it radiates destructively interferes with the output waveform traveling through the open unit cell at the selected frequency. For the purposes of this study, this metasurface can be considered as a passive noise-canceling device operating at a single frequency.

B. Active Noise Control System

The ANC system consists of two key components – the loudspeakers used to implement control and the microphones used to monitor the sound field in the waveguide. The control system, as described in Appendix B, uses the downstream microphone signals to determine the optimal loudspeaker drive signals in order to control the downstream sound field and maximize the transmission loss of the system. The primary sound field to be controlled is generated by a primary source located at the end of the waveguide, as shown in Fig. 1, which is driven via a Wondom Class D Audio Amplifier (Sure Electronics AA-AB32155) with a Gaussian white noise signal with a standard deviation of 1 Volt. The following subsections describe the loudspeaker and microphone arrangements used in the ANC system.

1. Loudspeakers

The metasurface described in the previous section has been augmented using an array of 9 miniature loudspeakers to form an active-passive MS, as shown in both Fig. 1. and Fig. 3b. The utilized loudspeakers were rated as 32 ohm, 500 mW drivers with a 23 mm diameter (model: MCABS-231-RC by multicompPRO). These transducers were chosen to meet the height limitation of the waveguide and lateral opening of the metasurface unit cells, and to have a frequency response covering the bandwidth of the designed metasurface. Each transducer was housed in a 3D-printed enclosure, designed to match the channel dimensions and wall thickness of the metasurface (shown in red, in Fig. 3b). The loudspeaker units were designed with an alternating arrangement, as also shown in Fig. 3b, to match the unit cell arrangement of the metasurface. Specifically, three loudspeaker configurations have been investigated: firstly, with the loudspeakers posterior to the open unit cells (Fig. 3c); secondly, with the loudspeakers anterior to the open unit cells (Fig. 3d); and finally, with the loudspeakers posterior to the labyrinthine unit cells (Fig. 3e). The loudspeakers could not be placed anterior to the labyrinthine cells of the metasurface due to their narrow geometry.

2. Microphones

The minimum number of microphones required for ANC has been determined using the modal decomposition approach proposed by Zhang *et al.* [25]. As described in Appendix A, this method allows the propagating modes (along the x-dimension) within a 2D-waveguide to be detected and is therefore much simpler than the raster scanning method employed in other works [8, 19]. This method uses white noise to excite the waveguide, thus allowing for a large bandwidth to be analyzed. The method proposed in [25] also allows the transmission and reflection coefficients for all modes within the considered frequency range of the experiment to be obtained.

As described in Appendix A, a total of 40 sensors are needed to ensure that the modal matrix is overdetermined. Therefore, 20 electret microphones (PCB Piezotronics, Model 130F20) were placed upstream of the MS, and 20 located downstream. The general locations of these sensors are depicted in Fig. 1a and the specific optimized locations are described in Appendix A and shown

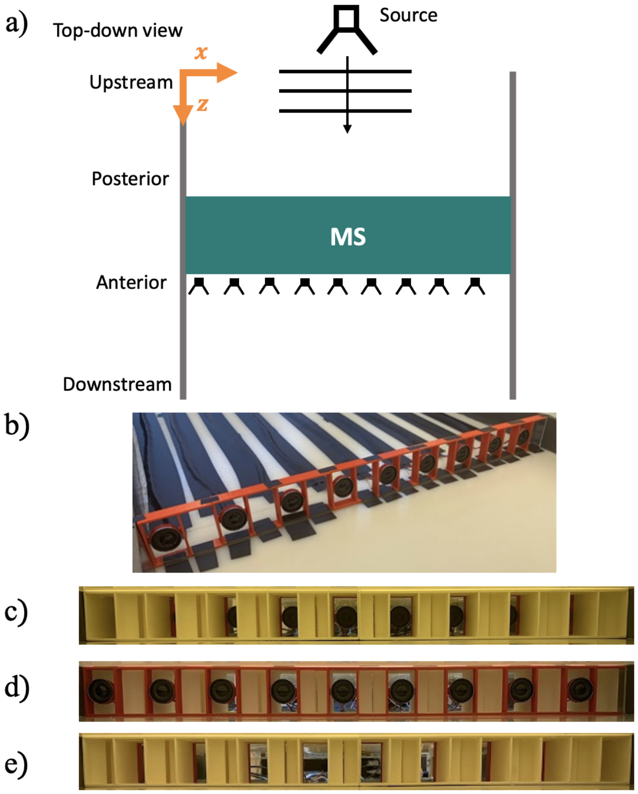

FIG. 3: (a) The general top-down view of the waveguide depicting the source location and positions of the metasurface and loudspeaker units for active control. (b) The loudspeaker array utilized in the active control implementation. (c) The hybrid metasurface with the loudspeakers placed posterior to the open unit cells. (d) The hybrid metasurface with the loudspeakers placed anterior to the open unit cells. (e) The hybrid metasurface with the loudspeakers placed posterior to the labyrinthine unit cells.

in Fig. A2. The microphones were connected to a National Instruments CompactDAQ cDAQ-9178, shown in Fig. 1a, which sends the time domain microphone signals to MATLAB.

III. PASSIVE PERFORMANCE

This section presents measurements of the passive attenuation provided by both the undriven or passive loudspeaker array within the waveguide and the hybrid labyrinthine metasurfaces, shown in Fig. 3. The measured passive performance is evaluated in terms of the transmission of the 0^{th} order propagating mode from 1 kHz to 3 kHz in steps of 5 Hz. Fig. 4 shows the transmission coefficient for the empty waveguide, the passive loudspeaker array and the passive metasurface with the loudspeakers located in the three possible configurations described in Section II B 1. It is important to first note from the results presented in Fig. 4 that a numerical error arises at 1715 Hz; this is due to poor conditioning of the modal matrix used to obtain the propagating plane wave component via the modal decomposition method detailed in Appendix A following Zhang *et al.* [25]. Although the conditioning of this problem can be improved via regularization techniques, since the numerical error occurs at a frequency below the range of interest for the designed metasurface, it has not been considered further.

The results presented in Fig. 4 reveal that the transmission of the empty waveguide is not exactly unitary, which can be associated with the thermo-viscous losses and the damping within the waveguide itself. It can also be seen from Fig. 4 that the insertion of the passive loudspeaker array introduces a small decrease in the transmission of the wave. Specifically, at frequencies between 1 kHz and 2 kHz the transmission of the 0^{th} propagating mode is around 90% with the loudspeaker array, and gradually decreases above 2 kHz to reach around 85% as the frequency approaches 3 kHz. This can be related to the absorption being provided by the passive components of the loudspeaker array (i.e. the materials of the loudspeaker and the plastic housing) and to reflection from the loudspeaker array as the wavelength decreases.

Fig. 4 also shows the passive transmission performance of the metasurface with the loudspeaker array in the three configurations shown in Fig. 3. Within the 1-2 kHz bandwidth, the introduction of the metasurface results in nearly 10% more of the incident wave being reflected or absorbed compared to the passive transmission through the loudspeaker array alone. A further dip in the transmission can be observed in Fig. 4 for the three passive metasurface-loudspeaker configurations between 2000 and 2250 Hz, which defines the operating bandwidth of the passive metasurface. For the two configurations with the loudspeakers in the posterior position, the bandwidth of the metasurface is relatively consistent. However, there is a small shift in the resonant peak – from 2125 Hz to 2180 Hz – when comparing the two posterior responses (blue and red) to the anterior response (pink). Additionally, the level and bandwidth of transmission loss with loudspeakers anterior to the open cells is not as significant as in the two posterior loudspeaker variations. At frequencies above the operational bandwidth of the passive hybrid metasurface, the transmission loss depends on the relative position of the loudspeakers: when the loudspeakers are posterior to the labyrinthine cells, the transmission decreases with increasing frequency, reaching around 70% at 3 kHz; when the loudspeakers are either posterior or anterior to the open unit cells, the transmission stays constant at around 80%. Note that the resonance for both posterior hybrid metasurface configurations will be referred to as 2125 Hz moving forward.

It is worth discussing the difference between the measured (2125 Hz) and designed (2400 Hz) interference frequency of the passive metasurface. This difference can

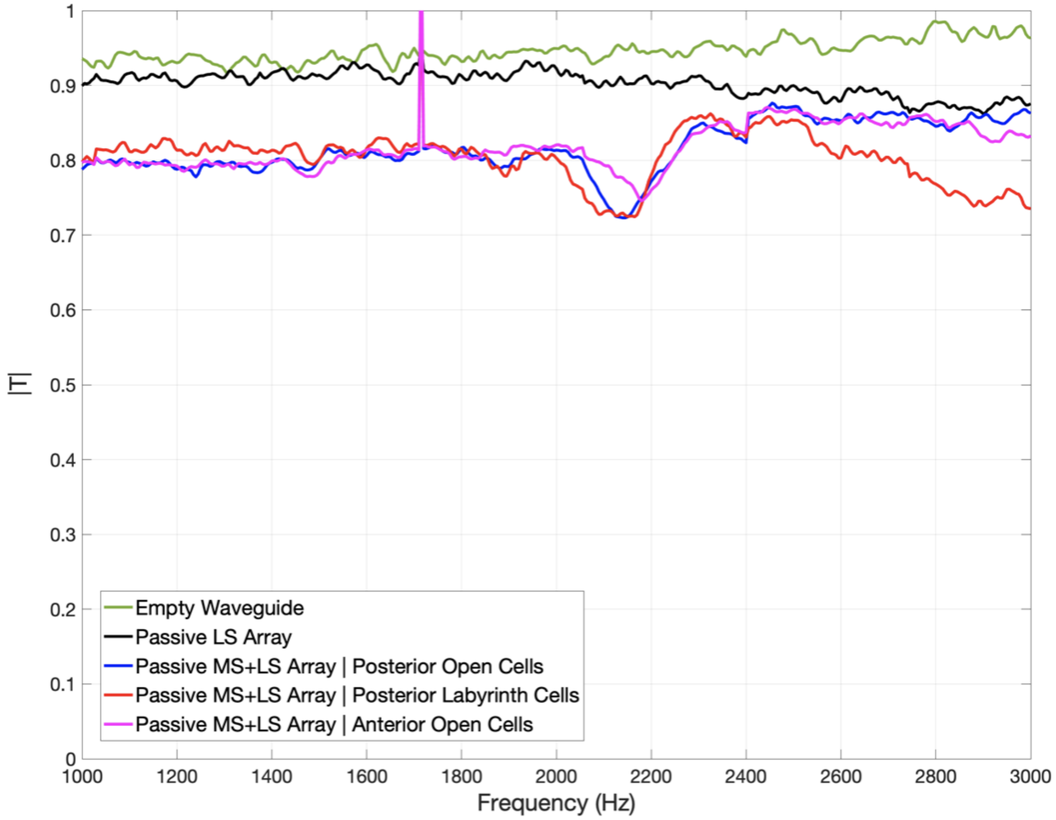

FIG. 4: Measured passive transmission coefficient corresponding to the 0^{th} propagating mode within the waveguide for an empty waveguide (green), standalone loudspeaker array (black), metasurface and loudspeaker hybrid system: loudspeakers posterior to the open cells (blue), loudspeakers posterior to the labyrinthine cells (red), and loudspeakers anterior to the open cells (pink). Note that “LS” is the abbreviation for loudspeaker.

be related to the additional path length introduced in the experimental realization due to the loudspeaker array, which decreases the resonant frequency at which effective interference between the open and labyrinthine unit cells occurs. To support this hypothesis, 2D and 3D simulations were performed (using the Acoustics Module in COMSOL Multiphysics) to explore the effect of the additional thickness introduced by the inclusion of the loudspeaker array. The 3D simulation results, reported in Appendix C, show a similar decrease in the resonance frequency of around 400 Hz when the loudspeaker array is introduced either anterior or posterior to the metasurface. The difference between the simulated and measured shift in frequency can be attributed to the approximations used in the simulations (e.g. the loudspeakers were modeled as hard objects) and to the higher-order physics interaction between the electroacoustic devices and the metasurface.

IV. ACTIVE PERFORMANCE

Having demonstrated the passive transmission performance of the hybrid metasurfaces in the previous section, this section presents an investigation into their active performance. Since there was no significant difference in the transmission of the 0^{th} propagating mode with the loudspeaker array positioned either posterior or anterior to the open unit cells of the metasurface, the hybrid performance is explored here only for the two cases where the loudspeakers are posterior to the open or the labyrinthine unit cells. Furthermore, to provide context to the additional performance achieved by the proposed hybrid metasurfaces, the active performance realized by the loudspeaker array in isolation is also analyzed.

In all three active cases, control is realized using an optimal multichannel feedforward active control system and is simulated offline using the responses measured from the experimental system. This approach allows the physical limits on control performance to be investigated, without introducing the complexities of a real-time implementation which are well understood [26]. The assumed feedforward control strategy, which is introduced in Appendix B, calculates the signals required to drive the array of loudspeakers to minimize the sum of the squared pressures measured at the array of downstream microphones. The active control algorithm also includes a constraint on the control effort, which is defined as the

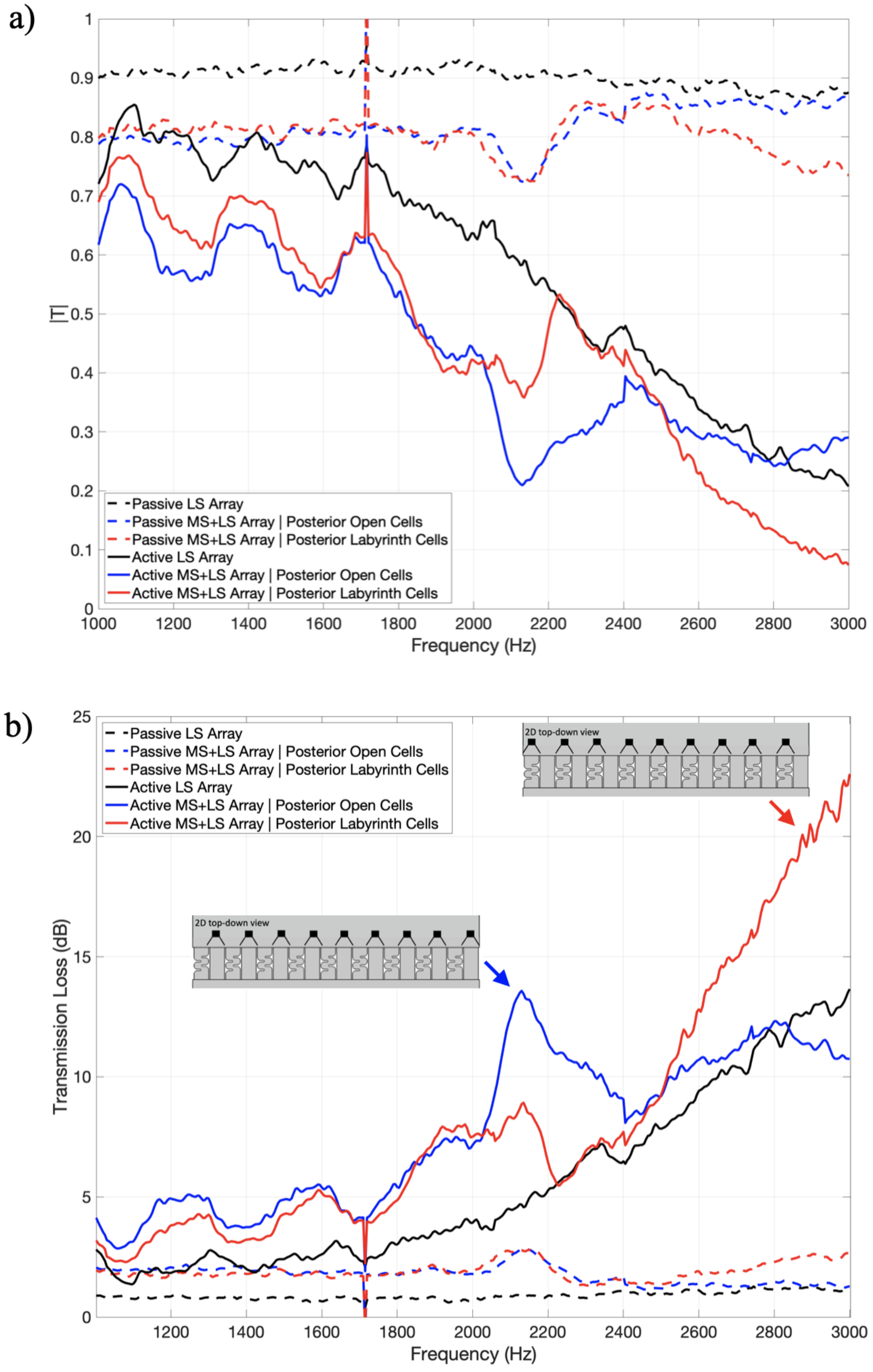

FIG. 5: Transmission coefficient (a) and transmission loss (b) corresponding to the 0^{th} propagating mode within the waveguide. Three passive cases are presented without active control—loudspeaker array (dashed black), hybrid metasurface with loudspeakers: posterior to labyrinthine cells (dashed red) and posterior to open unit cells (dashed blue). The analogous offline active control results are also given—loudspeaker array (solid black), hybrid metasurface with loudspeakers: posterior to labyrinthine cells (solid red) and posterior to open unit cells (solid blue). Overlaid in (b) are the 2D geometric views of the two hybrid systems analyzed for active control.

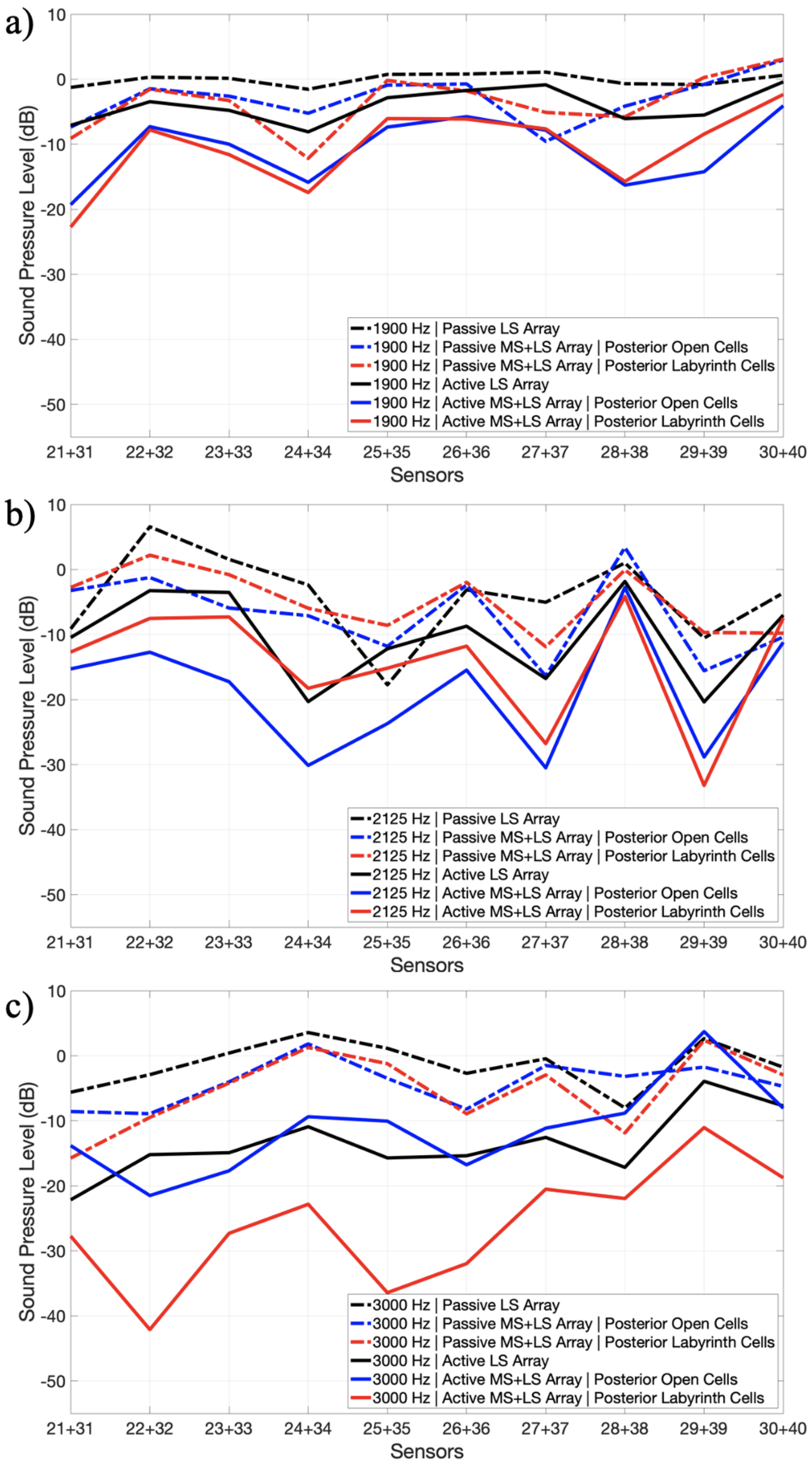

FIG. 6: The average sound pressure level at the downstream sensor pairs (adjacent microphones along the z-dimension) in decibels normalized to the pressure measured in the empty waveguide. (a) 1900 Hz: frequency where the active hybrid metasurfaces have similar transmission loss performance. (b) 2125 Hz: frequency where the hybrid metasurface with loudspeakers posterior to the open cells has the greatest transmission loss. (c) 3000 Hz: frequency where the active hybrid metasurface with loudspeakers posterior to the labyrinthine cells has the greatest transmission loss. Each plot has the same passive and active measurements as Fig.5.

sum of the squared magnitudes of the control signals driving the loudspeakers, as given by Eq. B3. It is necessary to constrain the control effort in practice to avoid overdriving the loudspeakers, but also to make the controller robust to real-world uncertainties. A control effort constraint is imposed here so that the control signals driving the loudspeakers are realizable in practice, but also to ensure that the required control effort is consistent between the three considered active systems.

Fig. 5 presents the transmission and transmission loss respectively of the three passive systems previously presented in Section III along with the three active systems, including the two hybrid metasurfaces, and the standalone active loudspeaker array. Transmission loss (TL) is defined as

$$TL = 20\log_{10}(1/|T|)\,, \qquad (1)$$

where $|T|$ is the magnitude of the transmission coefficient. Firstly, the active control algorithm was applied to the standalone loudspeaker array, placed in the posterior position relative to the metasurface (although the passive metasurface itself has been removed), and the resulting performance is shown by the solid black lines in Fig. 5. Comparing these results to the performance of the passive loudspeaker array shows that a significant reduction in the transmission is achieved by the active system, particularly at frequencies above 2 kHz. This result is slightly curious from the perspective of active control, which is generally more effective at lower frequencies, but may be related to the fact that only the 0^{th} order propagating mode is being considered here. Nevertheless, it is clear from these results that the active system using the loudspeaker array in isolation does exhibit a transmission loss that increases between 1 kHz and 3 kHz by around 11 dB, compared to a 1 dB increase for the passive loudspeaker array (dashed black line). It is also worth noting that at the 2125 Hz resonance of the hybrid metasurfaces, the transmission loss for the active loudspeaker array is 4 dB, which is an increase of around 3 dB compared to the passive attenuation provided by the loudspeaker array at this frequency. Fig. 5 also shows the performance of the two active hybrid metasurfaces, with the loudspeaker posterior to either the open or labyrinthine unit cells (solid blue and red lines respectively). In both cases, the hybrid metasurfaces significantly outperform both their respective passive responses (dashed blue and red lines) and the purely active system. An important note is that the two hybrid metasurfaces do not achieve the same active performance, even at frequencies where the passive performance is quite similar, which highlights a difference in the interaction between the active and passive components of the system.

To discuss the performance of the two hybrid metasurfaces in more detail, it is helpful to consider the behavior within three distinct frequency bands: below the passive metasurface interference band ($f < 2$ kHz); within the passive metasurface interference band (2 kHz $< f <$ 2.25 kHz); and above the passive metasurface interference band ($f > 2.25$ kHz). To support this analysis, Fig. 6 shows the average sound pressure level at the downstream sensor pairs across the width of the waveguide for the six passive and active system configurations at three distinct frequencies, corresponding to: 1900 Hz, where the two active hybrid metasurfaces have a similar transmission loss; 2125 Hz, where the hybrid metasurface with the loudspeakers posterior to the open cells achieves a high transmission loss; and 3000 Hz, where the hybrid metasurface with the loudspeakers posterior to the labyrinthine cells achieves a high transmission loss. At frequencies below the passive metasurface interference band, the two hybrid metasurfaces achieve quite consistent active performance, with an average transmission loss of around 6 dB, as shown in Fig. 5, and a similar SPL trend across all downstream sensor pairs, as shown in Fig. 6a. The hybrid systems also provide a significant performance advantage compared to the purely active system over this lower frequency bandwidth, with an increase in the transmission loss of up to 3 dB. However, it is notable that the active loudspeaker array achieves more consistent attenuation across all downstream sensors relative to the equivalent passive case compared to the hybrid systems. Note that the sensor pairs are taken as one microphone adjacent to another along the z-dimension (e.g. sensors 21 and 31 are a pair), Fig. A2 aids in illustrating the sensor pairs.

At frequencies around the passive metasurface interference band (2125 Hz), the hybrid system with the loudspeakers posterior to the open unit cells achieves the highest active performance, with a transmission loss of 13 dB (Fig. 5b), while the hybrid metasurface with the loudspeakers positioned posterior to the labyrinthine unit cells achieves a maximum transmission loss in this bandwidth of 9 dB. It can be observed from the sound pressure levels presented in Fig. 6b that while the passive hybrid metasurfaces (dashed blue and red) result in similar trends in the pressure field, there is a significant difference in their respective active results (solid red and blue). In particular, with the loudspeaker posterior to the open cells a greater attenuation in the sound pressure level at sensor pairs from 21+31 to 27+37 is achieved. Finally, at frequencies above the passive metasurface interference band, the hybrid system with the loudspeakers posterior to the open unit cells achieves a performance consistent with the purely active system, with a maximum transmission loss of 12 dB (Fig. 5b) and consistent sound pressure levels across the waveguide (Fig. 6c). In the same frequency band, the transmission loss achieved by the metasurface with the loudspeakers posterior to the labyrinthine unit cells increases at a greater rate than the other active systems, providing a transmission loss up to 11 dB greater than the other hybrid metasurface configuration. This performance advantage is also clearly demonstrated by sound pressure level across the waveguide shown in Fig. 6c, where a greater level of attenuation in the sound pressure is achieved across the downstream sensors for this hybrid metasurface.

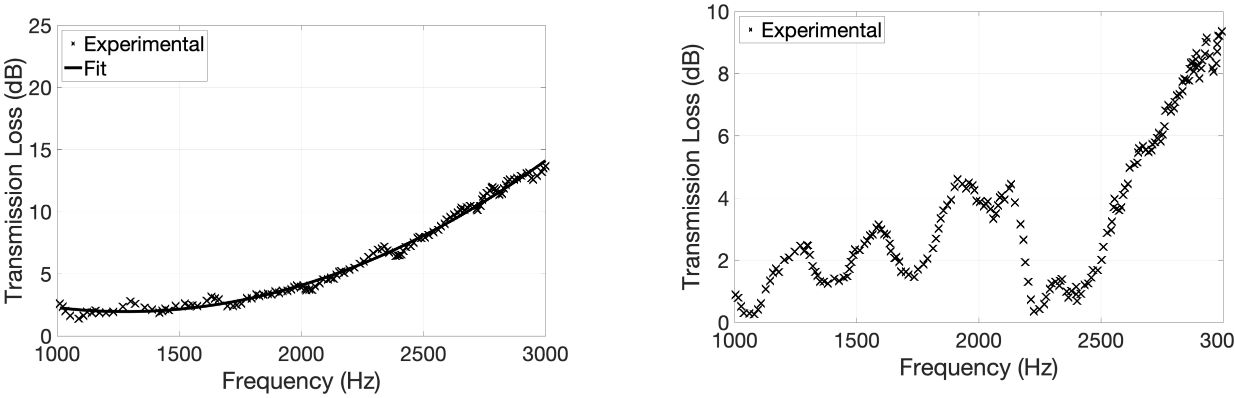

(a) Background TL and 2nd degree polynomial fit.

(b) Signal data for the metasurface with the loudspeakers posterior to the labyrinthine cells.

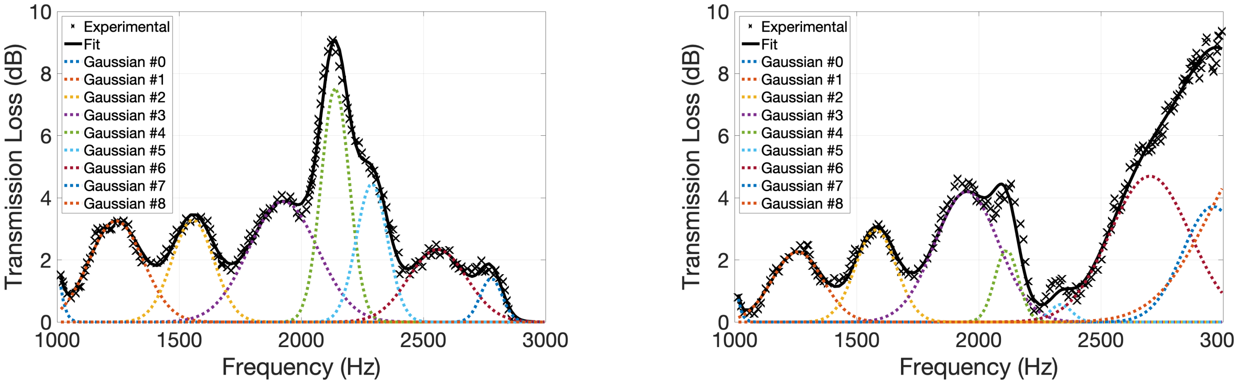

(c) Multi-peak fit for the metasurface with the loudspeakers posterior to the open cells.

(d) Multi-peak fit for the metasurface with the loudspeakers posterior to the labyrinthine cells.

FIG. 7: A schematic of the implemented spectroscopy analysis: (a) background fit; (b) signal data; (c) multi-peak fit for the metasurface with the loudspeakers posterior to the open cells; (d) multi-peak fit for the metasurface with the loudspeakers posterior to the labyrinthine cells.

TABLE I: Amplitude, frequency and Full Width at Maximum Height (FWMH) Coefficients of the multi-peak Gaussian functions shown in Fig. 7c and d. Uncertainties (not reported) were approximately 10% of the coefficient values.

	Peak 0	Peak 1	Peak 2	Peak 3	Peak 4	Peak 5	Peak 6	Peak 7	Peak 8
Amplitude (dB)	7	3	3	4	8	4	2	1	n.a.
Frequency (Hz)	940	1242	1556	1926	2139	2289	2558	2778	n.a.
FWMH (Hz)	56	157	121	200	82	90	169	63	n.a.

(a) Coefficient values for the metasurface with the loudspeakers posterior to the open cells.

	Peak 0	Peak 1	Peak 2	Peak 3	Peak 4	Peak 5	Peak 6	Peak 7	Peak 8
Amplitude (dB)	7	2	3	4	2	1	5	4	6
Frequency (Hz)	940	1258	1578	1951	2114	2335	2701	2959	3164
FWMH (Hz)	51	146	117	185	68	63	233	176	314

(b) Fitting values for the metasurface with the loudspeakers posterior to the labyrinthine cells.

The results presented for both hybrid metasurface configurations demonstrate a significant performance advantage compared to traditional ANC, both in the frequency band for which the passive metasurface is designed and beyond. However, the differences in performance between the two hybrid metasurfaces highlight a variation in the coupling between the loudspeakers and the passive metasurface in the two cases. To explore the potential underlying physical nature of the coupling mechanisms, the measured data has been analyzed using the techniques of optical/impedance spectroscopy [27]. To this end, the following methodology has been followed:

1. Assuming that the active loudspeaker array configuration corresponds to the background performance, i.e. that the hybrid systems can achieve at least this level of performance, a polynomial is fitted to the observed transmission loss. It was found that a 2nd degree polynomial was sufficient, such that

$$TL_{fit} = 4 \times 10^{-6} \cdot f^2 - 0.0105 \cdot f + 8.71 \,, \qquad (2)$$

where f is the frequency in Hz. The resulting transmission loss curve is compared to the measured background data in Fig. 7a.

2. TL_{fit} is then subtracted from the active transmission loss for the two hyrbid metasurface configurations to provide the so-called 'signal data' – see e.g. Fig. 7b for the case with the loudspeakers posterior to the labyrinthine cells. This approach assumes that the transmission loss achieved by the hybrid metasurfaces can be described starting from the underlying purely active system.

3. Finally, using the Peak Finder function in OriginPro (OriginLab, version 2025b) the obtained curves were fit with multiple Gaussian peaks. The algorithm found 13 peaks, but those with uncertainty lower than their amplitude, or with an amplitude lower than the background were excluded, leaving nine peaks. The resulting Gaussian functions are shown in Fig. 7c and Fig. 7d for the two hybrid metasurface configurations and the corresponding coefficients are detailed in Table I.

From the coefficient values shown in Table I, it can be observed that the transmission loss spectra for the two hybrid metasurfaces show two important features:

1. A single peak (#4) at 2125±20 Hz, with an average FWMH (Full Width at Maximum Height) of 70 Hz, which can be attributed to the metasurface.

2. A periodic series of peaks separated by 285±60 Hz, which can be attributed to resonances of the system (e.g. modes related to the geometry of the waveguide).

The efficiency of absorbing energy through the peak at 2125 Hz depends on the configuration, with the transmission loss at this frequency being more effective when the loudspeakers are posterior to the open cells. When the loudspeakers are positioned posterior to the labyrinthine cells, the energy transfer mechanism appears to change, with the energy initially transferred to Peak 4 being redistributed to peaks at higher frequencies and in fact an additional peak of the periodic system (i.e. Peak 8 at 3164 Hz) being required to complete the fit.

There are, however, two further key observations:

1. If the periodic series of resonances is a feature of the system geometry, it should also appear in the "active control only" case, but it was not possible to isolate it in that case. This energy transfer phenomenon is only visible when the metasurface is present, and this observation justifies the use of the "active control only" data as "background".

2. In the metasurface with the loudspeakers posterior to the open cells, the difference between the signal and the background is negative above 2860 Hz. Once again, if the periodic series of peaks were a feature of the system, it should also appear above 2860 Hz.

These two observations suggest that a different underlying physics is required to describe the behavior of the hybrid system. The coupling between a single-line/narrowband resonator (i.e. the metasurface) and a system capable of finding solutions at multiple frequencies, almost continuously (i.e. the ANC system) has been described by Fano in 1961 [28], in the case of two electronic configurations of a He atom. As shown in more recent studies [29], however, this type of interaction can lead to two regimes: one of weak coupling, where the response appears like a single peak over an existing trend, and one of strong coupling, where the single narrowband peak splits and two peaks appear, separated in frequency and introducing a change in the trend. Considering the hybrid metasurface with the loudspeakers posterior to the open cells, the results are characteristic of a weak-coupling regime, with the trend outside the narrowband metasurface region (∼2125 Hz) being similar to the one obtained with the purely active system, only with an enhancement of its periodic response. Instead, in the case where the loudspeakers are posterior to the labyrinthine unit cells, the performance appears to be described by a strong-coupling regime, with the presence of two peaks. One peak has been shifted to a frequency lower than 2125 Hz and the other above 3000 Hz. As shown in Appendix D, the theory in [29] explains the different heights of the peaks in Table I with a probability of at least 88%, thus confirming a change in the coupling regime between the two hybrid metasurface configurations. A deeper understanding of how to pilot these couplings (which in atomic physics are called "polaritons" [29]) will be the subject of future studies.

V. CONCLUSIONS

In this work, an investigation into the attenuation of wave transmission using "hybrid" metasurfaces, realized by combining a multichannel feedforward active control system with a passive labyrinthine acoustic metasurface has been presented. Modal decomposition was utilized to analyze the transmission of the 0^{th} mode propagating in a rectangular waveguide, for the cases of the passive hybrid metasurfaces, traditional ANC and two hybrid metasurface configurations. Both active hybrid metasurfaces outperformed their respective passive responses and the purely active system, demonstrating the advantages offered by hybrid systems for broadband noise management applications. The presented results show evidence that it is possible to modify the physical coupling between an active control system and metamaterial simply by changing the positions of the loudspeakers relative to the metasurface. Like in passive metamaterials, geometrical and design choices may result in performance changes, opening a new design discipline for active metamaterials.

This research has shown that the hybrid metasurfaces offer a synergistic performance advantage, with the performance exceeding that offered by the simple linear summation of the passive metasurface and the traditional active control system over different frequency ranges depending on the selected configuration. As well as investigating real-time implementation of the proposed hybrid metasurfaces, it will also be important to further optimize the metasurface to maximize the transmission loss. For example, exploring the potential performance when loudspeakers are located behind a combination of labyrinthine and open unit cells may combine the synergistic performance advantages offered by the two hybrid configurations investigated in this work. Additionally, further work is required to investigate the coupling between the active control system and the metasurface, to further explore the concept of "polaritons" within this acoustic metasurface context, potentially allowing greater leverage of the strong attenuation outside the resonant bandwidth of the active metasurface.

VI. ACKNOWLEDGMENTS

Gregory Hernandez thanks the US-UK Fulbright Commission for providing him the opportunity to study abroad and propose this research at the ISVR. Greg also thanks Ze Zhang for their help in assisting with the modal decomposition analysis. Gianluca Memoli acknowledges funding through his collaboration with Metasonixx Ltd. Jordan Cheer was partially supported by the Department of Science, Innovation and Technology (DSIT) Royal Academy of Engineering under the Research Chairs and Senior Research Fellowships programme.

DATA AVAILABILITY

The data in this paper is available on the repository Zenodo: https://doi.org/10.5281/zenodo.18049410.

Appendix A: Modal Decomposition

This appendix reviews the theoretical analysis necessary to obtain the modal information of the 2D-waveguide deployed in this paper. This modal decomposition follows the derivations by Zhang *et al.* [25].

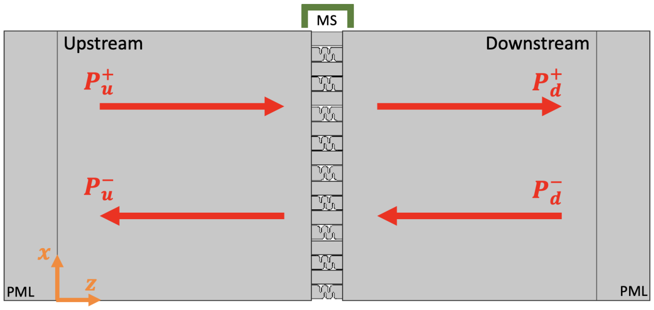

FIG. A1: A schematic of the scattering matrix variables overlaid on the 2D COMSOL rendering of the waveguide with the metasurface inserted (indicated by MS). PML is the perfectly matched layer that allows continuous propagation in the z-direction.

The frequency range in this paper extends from 1 kHz to 3 kHz. Based on the dimensions of the waveguide (W: 50 cm, L: 100 cm, H: 4.5 cm), there are 8 cut-on modes along the x-dimension as depicted in Fig. A1 within this bandwidth. The first cut-on mode in the y-direction is at 3.81 kHz (dimension out of the page in Fig. A1). The modes can propagate along the z-axis and the modal matrix derived by Zhang *et al.* accounts for the surface area impedance mismatch at both ends of the waveguide [25]. Note that the modal matrix contains the pressure pattern of the wave along the cross-section of the waveguide and the propagating wave information based on the wavenumber [25]. The metasurface (MS) shown in Fig. A1 partitions the waveguide into two sections—upstream and downstream. The pressure amplitudes and direction of the propagating modes are depicted by the red arrows in Fig. A1 where $P_u^{\pm}$ and $P_d^{\pm}$ are the pressure amplitudes of each mode—± indicates positive or negative direction given by the coordinate system in Fig. A1, and the subscripts u, d refer to either the upstream or downstream section. Equation A1 relates the pressure amplitudes of each upstream and downstream mode to one another through the scattering matrix $\underline{S}$, such that

$$\begin{bmatrix} \underline{P_d^+} \\ P_u^- \end{bmatrix} = \begin{bmatrix} \underline{T^+} & \underline{R^-} \\ \underline{R^+} & \underline{T^-} \end{bmatrix} \begin{bmatrix} \underline{P_u^+} \\ P_d^- \end{bmatrix} = \underline{S} \begin{bmatrix} \underline{P_u^+} \\ P_d^- \end{bmatrix}. \tag{A1}$$

The matrices $\underline{T^{\pm}}$ and $\underline{R^{\pm}}$ represent the transmission and reflection coefficients for the different modes with positive and negative z-direction incidences [25]. The modal matrix derived by Zhang *et al.* requires $s = 2N$ independent measuring positions (s being the number of microphones). The scattering matrix ($\underline{S}$) is of size $2N$x$2N$ where N is the number of cut-on modes [25]. Since there are 8 cut-on modes being considered, there must be at least 18 microphones on one side of the waveguide to capture all pressure amplitudes (this accounts for the plane wave, or 0^{th} propagating mode, too), and at least 18 independent measurements to obtain the scattering matrix $\underline{S}$. Therefore, the implemented experiment utilized a total of 40 microphones (20 upstream and 20 downstream in the waveguide) and 22 independent measuring positions (split evenly between the upstream and downstream sections of the waveguide) to make the modal and scattering matrices overdetermined.

The scattering matrix is further defined as

$$\underline{S} = \begin{bmatrix} P^{+}_{d,0,1} & \cdots & P^{+}_{d,0,2N} \\ \vdots & & \vdots \\ P^{+}_{d,N-1,1} & \cdots & P^{+}_{d,N-1,2N} \\ P^{-}_{u,0,1} & \cdots & P^{-}_{u,0,2N} \\ \vdots & & \vdots \\ P^{-}_{u,N-1,1} & \cdots & P^{-}_{u,N-1,2N} \end{bmatrix} \begin{bmatrix} P^{+}_{u,0,1} & \cdots & P^{+}_{u,0,2N} \\ \vdots & & \vdots \\ P^{+}_{u,N-1,1} & \cdots & P^{+}_{u,N-1,2N} \\ P^{-}_{d,0,1} & \cdots & P^{-}_{d,0,2N} \\ \vdots & & \vdots \\ P^{-}_{d,N-1,1} & \cdots & P^{-}_{d,N-1,2N} \end{bmatrix}^{-1} , \tag{A2}$$

where in $P^{\pm}_{*,k,l}$, k represents the kth mode, and l denotes the lth measurement [25]. The elements of Eq. A2 depend upon the inversion of the modal matrix (Eq. 10 defined by Zhang *et al.* [25]).

To improve the precision of the scattering matrix estimation, the conditioning number of the modal matrix must be small. Since the modal matrix depends upon the microphone positions, they have been optimized here using **fmincon** in MATLAB [30] to improve the conditioning of the inverse problem. The objective function for reducing the conditioning of the modal matrix is defined as

$$F(x_m, z_m, f) = \frac{1}{N_{fb}} \sum_{i=1}^{N_{fb}} w_i(f) C(x_m, z_m, f)_i \, , \tag{A3}$$

where N_{fb} is the number of frequency bands in the frequency range of interest, i is the ith frequency band, w_i is the weighting factor in the ith frequency band, x_m and z_m are microphone locations, f is the discrete frequency within the ith band, and $C(x_m, z_m, f)_i$ is the linear average of the condition number in the ith frequency band defined as

$$C(x_m, z_m, f)_i = \overline{\mathbf{cond}(\underline{M}(x_m, z_m, f))_i} \, , \tag{A4}$$

where **cond** is the MATLAB operator for computing the condition number of a matrix [31], and $\underline{M}$ is the modal matrix given by Eq. 10 in Zhang *et al.* [25]. The weighting factor for each frequency band is

$$w_i = \frac{1}{N_2 - N_i + 1}, \tag{A5}$$

where N_2 is the number of cut-on modes at the maximum frequency in the bandwidth, and N_i is the number of cut-on modes within the ith frequency band [25].

The forty sensors within the realized experimental setup were split into four sets of ten with two pairs of twenty sensors on either side of the metasurface. To simplify the position optimization, only sensors 1-20 are optimized and their relative positions are mirrored on the opposite side of the metasurface to give the positions of sensors 21-40. The initial layout of the sensors are centrally located 20 cm away from the face of the metasurface, as indicated by the black crosses in Fig. A2 and separated by a distance of $\lambda_{max}/4$ where λ_{max} is the acoustic wavelength at the highest frequency. The dotted lines in Fig. A2 indicate the boundaries defining the sensor position optimization area. The sensor pairs (e.g. sensors 1 and 11) do not have to coincide along a parallel line relative to the z-axis.

The sensor positions after optimization are given as the colored circles in Fig. A2 and the coordinate positions are detailed in Table II. As a result of these optimized positions, the objective function defined in Eq. A3 decreased from an initial value of 2.08 to 0.87, strongly reducing numerical issues due to the presence of cut-on modes (e.g. as observed at 1715 Hz in Figs. 4 and 5).

Following this process, the absorption, transmission, and reflection coefficients corresponding to each mode can be determined via Eq. A2. The absorption coefficient, for example, is given by

$$\alpha_m = 1 - |\underline{S}_{(1:N,m)}|^2 - |\underline{S}_{((N+1):2N,m)}|^2 \, , \tag{A6}$$

where $\underline{S}_{(k,l)}$ represents the kth row and lth column of the scattering matrix $\underline{S}$ [25]. The transmission and reflection coefficients to various modes from the mth incident mode are given as $\underline{S}_{(1:N,m)}$ and $\underline{S}_{((N+1):2N,m)}$ respectively. Making use of the term $\underline{S}_{(1:N,m)}$ from Eq. A6, the transmission of the 0^{th} propagating mode in the positive direction, or plane wave, within the waveguide can be determined and this is the resulting transmission data presented in Figs. 4 and 5.

Appendix B: Multichannel Feedforward Active Control System

This second section introduces the multichannel feedforward active control algorithm that was applied to the loudspeaker-metasurface combination to create an active metasurface. A feedforward system senses a disturbance upstream from the control system and this disturbance is utilized as a reference signal for control at some error sensor(s) located downstream. The following equation generalizes a multichannel feedforward system

$$\mathbf{e} = \mathbf{d} + \mathbf{G}\mathbf{u}, \tag{B1}$$

where $\mathbf{e}$ is the vector of error sensors, $\mathbf{d}$ is the vector of disturbance signals, $\mathbf{G}$ is the matrix of complex plant responses, and $\mathbf{u}$ is the vector of control signals applied to the loudspeakers [32]. The plant response, $\mathbf{G}$, represents the transfer function between the error sensors and individual loudspeakers.

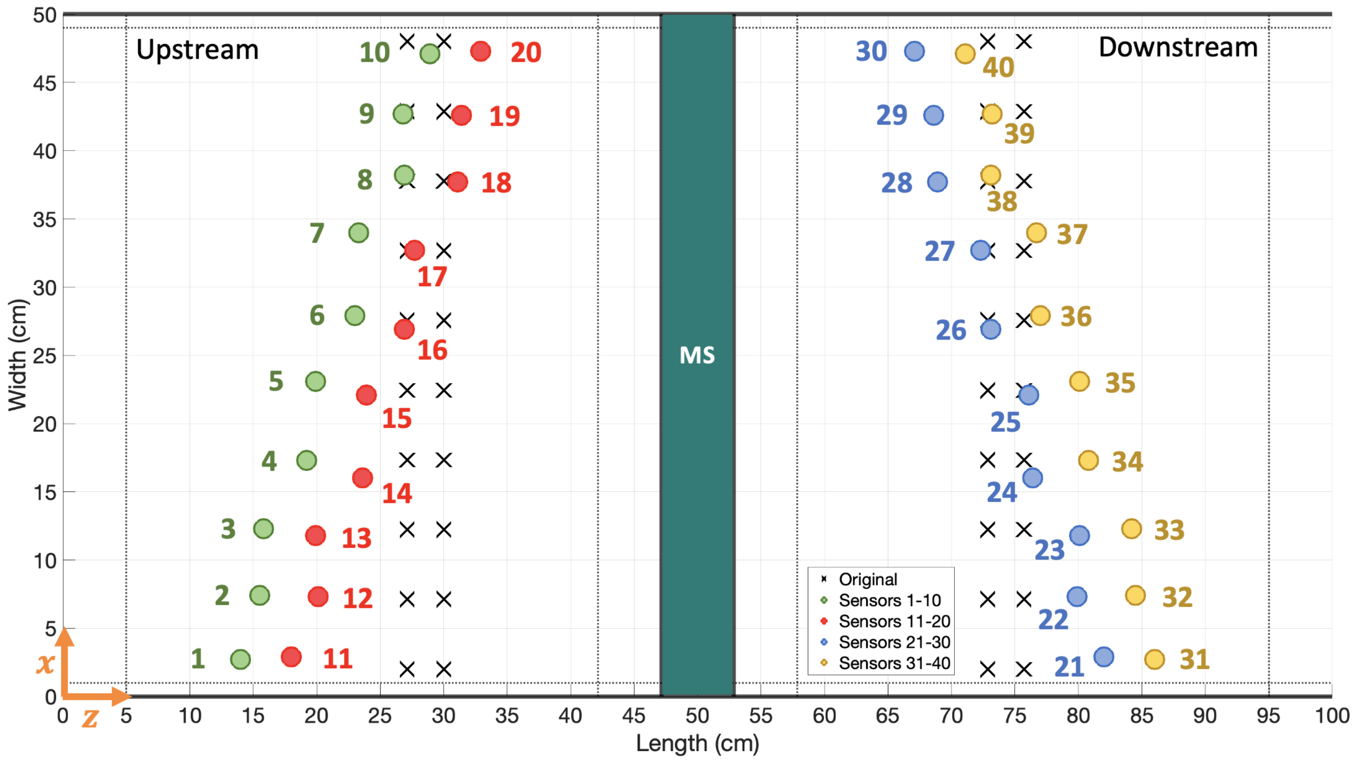

FIG. A2: The illustrated layout of the initial sensor positions (black crosses) and optimized locations (colored and numerated) in the 2D waveguide. Sensors 1-10 are the green circles, 11-20 are red, 21-30 are blue, and 31-40 are yellow. MS indicates the location of the metasurface being tested.

TABLE II: The optimized sensor positions that reduce the condition number of the modal matrix given by Eq. A2. These positions are illustrated in Fig. A2.

Sensor	1	2	3	4	5	6	7	8	9	10
x_m (cm)	2.7	7.4	12.3	17.3	23.1	27.9	34.0	38.2	42.7	47.1
z_m (cm)	14.0	15.5	15.8	19.2	19.9	23.0	23.3	26.9	26.8	28.9

(a) Optimized sensor positions. Sensors 1-10.

Sensor	11	12	13	14	15	16	17	18	19	20
x_m (cm)	2.9	7.3	11.8	16.0	22.1	26.9	32.7	37.7	42.6	47.3
z_m (cm)	18.0	20.1	19.9	23.6	23.9	26.9	27.7	31.1	31.4	32.9

(b) Optimized sensor positions. Sensors 11-20.

Sensor	21	22	23	24	25	26	27	28	29	30
x_m (cm)	2.9	7.3	11.8	16.0	22.1	26.9	32.7	37.7	42.6	47.3
z_m (cm)	82.0	79.9	80.1	76.4	76.1	73.1	72.3	68.9	68.6	67.1

(c) Optimized sensor positions. Sensors 21-30.

Sensor	31	32	33	34	35	36	37	38	39	40
x_m (cm)	2.7	7.4	12.3	17.3	23.1	27.9	34.0	38.2	42.7	47.1
z_m (cm)	86.0	84.5	84.2	80.8	80.1	77.0	76.7	73.1	73.2	71.1

(d) Optimized sensor positions. Sensors 31-40.

To determine the optimal control signals, it is necessary to define a cost function to be minimized, which in ANC is typically provided by the summation of the modulus squared error signals given as

$$J = \sum_{l=1}^{L} |e_l|^2 = \mathbf{e}^{\mathrm{H}}\mathbf{e}, \tag{B2}$$

where the superscript H is the Hermitian transpose, and

L is the number of error sensors [32]. In most physical systems, the loudspeakers have a power limiting factor which requires a constraint on the control effort to be introduced. The control effort is given as

$$P = \sum_{m=1}^{M} |u_m|^2 = \mathbf{u}^{\mathrm{H}}\mathbf{u}, \tag{B3}$$

which is related to the electrical power required to drive the loudspeakers, and M is the number of actuators used for active control [32]. The cost function given by Eq. B2 can then be modified to include a term proportional to the control effort

$$J = \mathbf{e}^{\mathrm{H}}\mathbf{e} + \beta\mathbf{u}^{\mathrm{H}}\mathbf{u}, \tag{B4}$$

where β is the regularization factor which is a positive real effort-weighting parameter [32]. The regularization factor is used to adjust the constraint on the control effort, which can limit the level of the control signals to be within the limitations of the selected loudspeakers and can also improve the robustness of the system to real-world uncertainty.

As mentioned, the objective of the active control system is to minimize the cost function defined by Eq. B4. The multichannel feedforward active control system considered here is overdetermined, since it has more error sensors than control sources and the optimal vector of control signals is thus given as

$$\mathbf{u}_{\mathrm{opt}} = -\left[\mathbf{G}^{\mathrm{H}}\mathbf{G} + \beta\mathbf{I}\right]^{-1}\mathbf{G}^{\mathrm{H}}\mathbf{d}, \tag{B5}$$

where $\mathbf{I}$ is the identity matrix with size $2M$x$2M$, and the matrix $\mathbf{G}^{\mathrm{H}}\mathbf{G}$ is assumed to be positive definite [32]. Note that the optimized control vector, and derivation of the aforementioned equations, are calculated based on frequency domain information. Eq. B5 is applied to Eq. B1 to evaluate the error signals in the downstream section of the waveguide. Eq. B5 is computed for each frequency (1 kHz to 3 kHz in steps of 5 Hz) for a chosen value of beta based on the control effort defined in Eq. B3. Since there are multiple independent primary sources used in the described modal decomposition approach, Eq. B5 is used to determine the optimal control signals for each measurement with a different regularization factor selected to limit the electrical power to within the operational limits of the practical loudspeakers. To determine a suitable regularization factor, the control effort corresponding to each individual loudspeaker, for a given primary source measurement, was compared to the rms voltage of the signal used to drive the loudspeakers during the measurements. The regularization factor was then chosen so that no single loudspeaker would exceed this defined voltage drive threshold.

Appendix C: 3D Simulation

Fig. A3 presents the geometry of the 3D simulation of the experimental setup implemented using COMSOL Multiphysics. The maximum element size for the mesh of the domain was chosen to be $\frac{1}{10}$ of the wavelength at the highest frequency (3 kHz). The waveguide was terminated on both ends with a perfectly matched layer (PML), which was used to approximate the open end termination in the real experimental configuration, and all other boundaries were chosen as sound hard boundaries. The excitation source was chosen to be a point monopole source. Simulations were run in steps of 5 Hz from 1000 Hz to 3000 Hz. Pressure responses were recorded using domain point probes, located at the microphone positions as described in Appendix A. Thermoviscous effects were not considered in the implemented model.

The 3D simulation transmission results for the metasurface (red) and the metasurface-loudspeaker variation with loudspeakers behind the open unit cells (blue) are presented in Fig. A4. The most important part of this plot is the noticeable shift in the resonance frequency: a difference of 400 Hz. This can be linked to the increase in the effective path length due to the addition of the loudspeaker array structure. Secondly, the transmission loss capabilities increased by 40% between the two metasurface cases with the passive metasurface-loudspeaker response outperforming the standalone metasurface transmission results. As mentioned in Section III, a plausible cause for the shift in the interference frequency and increase in passive attenuation of the hybrid metasurface in Fig. A4 is the passive electroacoustic coupling between the loudspeaker array and unit cells of the metasurface. It is also worth noting that the transmission coefficient results presented in Fig. A4 show the presence of higher-order cut-on modes, which could be addressed by further improving the conditioning of the modal matrix as outlined in Appendix A.

Appendix D: Exploring the two coupling regimes

Since the proposed hybrid system includes both a "resonant" (i.e. the metasurface) and a "continuum" (i.e. the active control) sub-system, the coupling between them can be described using a Fano model. In their recent work about systems that can be described with the Fano model, Zeb [29] showed that there is a single Fano resonance only when the coupling between the two sub-systems is weak. However, if the two sub-systems are strongly coupled, two peaks appear instead. According to Zeb [29], the transition between these two regimes is not abrupt, but a wider "weak" resonance evolves into two "thinner" peaks in the spectrum when the parameter commanding the coupling between the two sub-systems increases. As shown in Figure A5, which reports the amplitudes and frequencies of the peaks according to Table I, for the two experimental hybrid metasurface configurations considered here, the observed behavior is quite consistent with the description of weakly and strongly coupled resonances. Firstly, with the loudspeakers positioned posterior to the open cells,

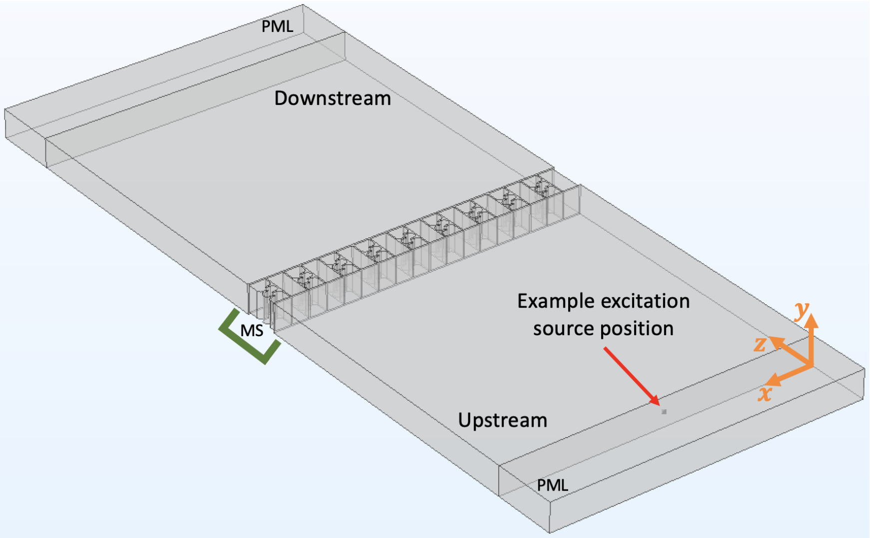

FIG. A3: COMSOL Multiphysics 3D geometry experimental setup with the metasurface placed at the center of the waveguide. MS indicates the metasurface and PML is the perfectly matched layer. An example source location (6/22) is added to illustrate how the waveguide was excited.

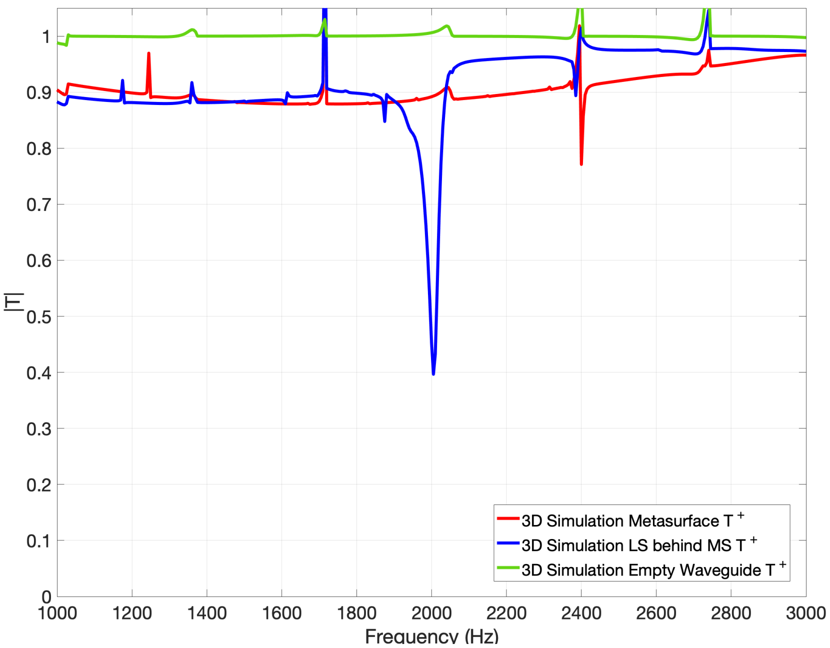

FIG. A4: The 3D simulation passive transmission results for the empty waveguide (green), metasurface (red) and loudspeaker-metasurface combination with the loudspeakers behind the open unit cells (blue).

the absorption near the resonance frequency of the hybrid metasurface increased: Peak 4 in Table I is 8 dB greater than observed for active control only and 7.8 dB greater than for the metasurface alone. This effect is slightly masked by the presence of a periodic spectrum, which has been attributed to the interaction between the size of the waveguide and the metasurface itself: when the loudspeakers are behind the open cells, Peak 3 and Peak 5 increase from 3 dB (which is the typical height of the other peaks in this spectrum) to 4 dB. Conversely, when the loudspeakers were posterior to the labyrinthine cells, there is very little energy in Peak 4 (2 dB) and Peak 5 (1 dB), while the energy in Peak 3, which is below the metasurface resonance, remains consistent (4 dB). This energy has been redistributed to Peak 6 (5 dB), Peak 7 (4 dB) and Peak 8 (6 dB), which all occur above the metasurface resonance frequency. To use technical jargon from molecular and atomic

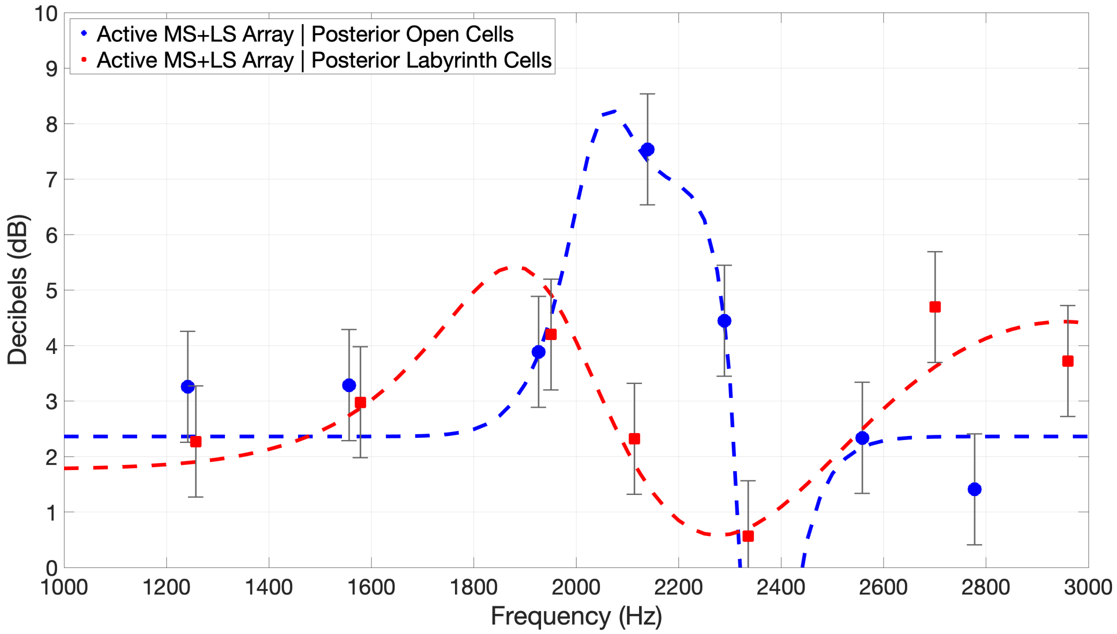

FIG. A5: The heights (and the frequencies) of the peaks from Table I in the two hybrid metasurface configurations and the corresponding fitting lines obtained using the equations in [29].

spectroscopy, the line relative to Peak 4 "split": part of the energy was distributed slightly below resonance and part above resonance. Based on these observations, it has been proposed that the parameter of coupling between the resonant and continuum sub-systems in the hybrid metasurface is controlled by the geometrical position of the loudspeakers relative to the two types of cells that make the metasurface.

To test this explanation, the equations from [29] have been fitted to the peaks of the systems as described in Section IV and the results are presented in Figure A5. In the hypothesis of a Gaussian interaction $V(f)$ centered around frequency f_0

$$V(f) = \Omega^2 \frac{1}{(2\pi\xi^2)^{1/2}} \exp\left(-\frac{(f-f_0)^2}{2\xi^2}\right). \tag{D1}$$

This means that the estimated peak data presented in Table I can be used to measure the coupling coefficient ξ/Ω from the shape of the Fano curve

$$\sigma(f) = \frac{(q+\epsilon)^2}{1+\epsilon^2} \tag{D2}$$

where σ is the absorption as a function of frequency, $\epsilon(f, f_0, \xi/\Omega)$ is a reduced energy parameter and q is an asymmetry parameter. To test the negative hypothesis (i.e. that the data does not follow this model) a χ^2 test has been used, which showed that:

- In the case where the loudspeakers are placed posterior to the open cells, the best-fit with the Fano model gives $q = -1.7$ and $\xi/\Omega = 1.1 \pm 0.1$, which corresponds to weak coupling. With $\chi^2 = 1.17$, the probability that the model from [29] does not describe the data is $p = 0.114$.

- In the case where the loudspeakers are placed posterior to the labyrinthine cells, the best-fit with the Fano model gives $q = -1.15$ and $\xi/\Omega = 0.61 \pm 0.06$, which correspond to the case of strong coupling. With $\chi^2 = 0.71$, the probability that the model from [29] does not describe the data is $p = 0.049$.

The theory in [29] therefore describes the data observed for the hybrid metasurface herein with a probability $p \geq 0.886$. Future studies may verify whether this framework could be used to interpret the behavior of other works from the literature that use a Fano-resonance model to describe complex acoustic systems that exhibit effects that depend on the position of the loudspeakers.

[1] World Health Organization, *Burden of disease from environmental noise* (WHO, 2011).
[2] F. Fahy, Foundations of engineering acoustics (Elsevier, London, 2001) Chap. 7, 4th ed.
[3] A. G. Bose and J. Carter, Headphoning, patent no. 4,455,675 (1984).

[4] T. J. Sutton, S. J. Elliott, M. McDonald, and T. J. Saunders, Active control of road noise inside vehicles, Institute of Noise Control Engineering (1994).

[5] S. J. Elliott, P. A. Nelson, I. M. Stothers, and C. C. Boucher, In-flight experiments on the active control of propeller-induced cabin noise, Journal of Sound and Vibration **140**, 219 (1990).

[6] P. A. Nelson and S. J. Elliott, *Active control of sound* (Academic, 1992) p. 436.

[7] S. A. Cummer, J. Christensen, and A. Alu, Controlling sound with acoustic metamaterials, Nature Reviews (2016).

[8] J. Li, W. Wang, Y. Xie, B.-I. Popa, and S. A. Cummer, A sound absorbing metasurface with coupled resonators, Applied Physics Letters **109** (2016).

[9] J. Li, A. Song, and S. A. Cummer, Bianisotropic acoustic metasurface for surface-wave-enhanced wavefront transformation, Physics Review Applied **14** (2020).

[10] G. Memoli, M. Caleap, M. Asakawa, D. R. Sahoo, B. W. Drinkwater, and S. Subramanian, Metamaterial bricks and quantization of meta-surfaces, Nature Communications (2017).

[11] B.-I. Popa and S. A. Cummer, Homogeneous and compact acoustic ground cloaks, Physical Review B **83** (2011).

[12] Y. Li and B. M. Assouar, Acoustic metasurface-based perfect absorber with deep subwavelength thickness, Applied Physics Letters **108** (2016).

[13] G. Ma, M. Yang, S. Xiao, Z. Yang, and P. Sheng, Acoustic metasurface with hybrid resonances, Nature materials **13**, 873 (2014).

[14] G. Liao, C. Luan, Z. Wang, J. Liu, X. Yao, and J. Fu, Acoustic metamaterials: A review of theories, structures, fabrication approaches, and applications, Advanced Materials Technologies **6**, 2000787 (2021).

[15] L. Sangiuliano, B. Reff, J. Palandri, F. Wolf-Monheim, B. Pluymers, E. Deckers, W. Desmet, and C. Claeys, Low frequency tyre noise mitigation in a vehicle using metal 3d printed resonant metamaterials, Mechanical Systems and Signal Processing **179**, 109335 (2022).

[16] F. Pires, R. F. Boukadia, M. Wandel, C. Thomas, E. Deckers, W. Desmet, and C. Claeys, Novel resonator concept for improved performance of locally resonant based metamaterials, Thin-Walled Structures **209**, 112866 (2025).

[17] G. Memoli, L. Chisari, L. Bonoldi, and A. A. E. Ouahabi, Bringing acoustic metamaterials to hospital noise, Acoustic Bullettin **47**, 42 (2021).

[18] B.-I. Popa, L. Zigoneanu, and S. A. Cummer, Tunable active acoustic metamaterials, Physical Review B **88** (2013).

[19] B.-I. Popa, Y. Zhai, and H.-S. Kwon, Broadband sound barriers with bianisotropic metasurfaces, Nature Communications (2018).

[20] J. Tan, J. Cheer, and S. Daley, Realisation of nonreciprocal transmission and absorption using wave-based active noise control, JASA Express Letters **2** (2022).

[21] J. Tan, J. Cheer, and C. House, Realisation of broadband two-dimensional nonreciprocal acoustics using an active acoustic metasurface, The Journal of the Acoustical Society of America **156**, 1231 (2024).

[22] J. Cheer, S. Daley, and C. McCormick, Feedforward control of sound transmission using an active acoustic metamaterial, Smart Materials and Structures (2017).

[23] F. Langfeldt and J. Cheer, Controlling the effective surface mass density of membrane-type acoustic metamaterials using dynamic actuators, The Journal of the Acoustical Society of America **153**, 961 (2023).

[24] G. Memoli, L. Chisari, J. P. Eccles, M. Caleap, B. W. Drinkwater, and S. Subramanian, Vari-sound: A varifocal lens for sound, in *Proceedings of the 2019 CHI Conference on Human Factors in Computing Systems*, CHI '19 (Association for Computing Machinery, New York, NY, USA, 2019) p. 1–14.

[25] Z. Zhang, H. Denayer, C. Claeys, W. Desmet, and E. Deckers, Angle-dependent reflection, transmission and absorption coefficients measurements using a 2d waveguide, Applied Acoustics **177** (2021).

[26] S. J. Elliott, *Signal processing for active control* (Academic, 2001) p. 511.

[27] E. Barsoukov and J. Ross Macdonald, *Impedance Spectroscopy: Theory, Experiment, and Applications* (Wiley, 2005).

[28] U. Fano, Effects of configuration interaction on intensities and phase shifts, Phys. Rev. **124**, 1866 (1961).

[29] M. A. Zeb, Fano resonance in the strong-coupling regime, Phys. Rev. B **106**, 155134 (2022).

[30] MATLAB, fmincon, `https://www.mathworks.com/help/optim/ug/fmincon.html` ().

[31] MATLAB, cond, `https://www.mathworks.com/help/matlab/ref/cond.html` ().

[32] S. Elliott, Signal processing for active control (Academic Press, 2000) Chap. 4, 1st ed.